64. George, E. L., Georges-Labouesse, E. N., Patel-King, R. S., Rayburn, H., and Hynes, R. O. (1993) Defects in mesoderm, neural tube and vascular development in mouse embryos lacking fibronectin. *Development* **119**, 1079-1091
65. Neptune, E. R., Frischmeyer, P. A., Arking, D. E., Myers, L., Bunton, T. E., Gayraud, B., Ramirez, F., Sakai, L. Y., and Dietz, H. C. (2003) Dysregulation of TGF-beta activation contributes to pathogenesis in Marfan syndrome. *Nature genetics* **33**, 407-411
66. Nistala, H., Lee-Arteaga, S., Smaldone, S., Siciliano, G., Carta, L., Ono, R. N., Sengle, G., Arteaga-Solis, E., Levasseur, R., Ducy, P., Sakai, L. Y., Karsenty, G., and Ramirez, F. (2010) Fibrillin-1 and -2 differentially modulate endogenous TGF-beta and BMP bioavailability during bone formation. *The Journal of cell biology* **190**, 1107-1121
67. Koli, K., Wempe, F., Sterner-Kock, A., Kantola, A., Komor, M., Hofmann, W. K., von Melchner, H., and Keski-Oja, J. (2004) Disruption of LTBP-4 function reduces TGF-beta activation and enhances BMP-4 signaling in the lung. *The Journal of cell biology* **167**, 123-133
68. Yoshinaga, K., Obata, H., Jurukovski, V., Mazzieri, R., Chen, Y., Zilberberg, L., Huso, D., Melamed, J., Prijatelj, P., Todorovic, V., Dabovic, B., and Rifkin, D. B. (2008) Perturbation of transforming growth factor (TGF)-beta1 association with latent TGF-beta binding protein yields inflammation and tumors. *Proc Natl Acad Sci U S A* **105**, 18758-18763
69. Loeys, B. L., Gerber, E. E., Riegert-Johnson, D., Iqbal, S., Whiteman, P., McConnell, V., Chillakuri, C. R., Macaya, D., Coucke, P. J., De Paepe, A., Judge, D. P., Wigley, F., Davis, E. C., Mardon, H. J., Handford, P., Keene, D. R., Sakai, L. Y., and Dietz, H. C. (2010) Mutations in fibrillin-1 cause congenital scleroderma: stiff skin syndrome. *Sci Transl Med* **2**, 23ra20
70. Mazzieri, R., Jurukovski, V., Obata, H., Sung, J., Platt, A., Annes, E., Karaman-Jurukovska, N., Gleizes, P. E., and Rifkin, D. B. (2005) Expression of truncated latent TGF-beta-binding protein modulates TGF-beta signaling. *Journal of cell science* **118**, 2177-2187
71. Ramirez, F., and Rifkin, D. B. (2009) Extracellular microfibrils: contextual platforms for TGFbeta and BMP signaling. *Curr Opin Cell Biol* **21**, 616-622
72. Altrock, E., Sens, C., Wuerfel, C., Vasel, M., Kawelke, N., Dooley, S., Sottile, J., and Nakchbandi, I. A. (2015) Inhibition of fibronectin deposition improves experimental liver fibrosis. *Journal of hepatology* **62**, 625-633
73. Muro, A. F., Chauhan, A. K., Gajovic, S., Iaconcig, A., Porro, F., Stanta, G., and Baralle, F. E. (2003) Regulated splicing of the fibronectin EDA exon is essential for proper skin wound healing and normal lifespan. *The Journal of cell biology* **162**, 149-160

Abbreviations

αSMA, α-smooth muscle actin; ALT, alanine aminotransferase; AFM, atomic force microscopy; BAPN, β-aminopropionitrile; BMP 1, Bone morphogenic protein 1; CCl_4, carbon tetrachloride; DAPI, 4'6-diamidino-2-phenylindole; ECM, extracellular matrix; FITC, fluorescein isothiocyanate; Fn, fibronectin; LAP, latency associated protein; LLC, large latent complex; LOX, lysyl oxidase; LTBP, latent TGF-β-binding protein; MMP, matrix metalloproteinase; mAb, monoclonal antibody; PCR, polymerase chain reaction; pAb, polyclonal antibody; pI-pC, polyinosinic-polycytidic acid; PVDF, polyvinylidene fluoride; TEM, transmission electron microscopy; TGF-β, transforming growth factor-β

Figure Legends

Fig. 1. Liver fibrosis/cirrhosis developing during CCl_4-induced (0.5 ml/kg weight) chronic liver injury is greater in mice lacking liver Fn (Control, wild-type with CCl_4; LivFn-null, mutant with CCl_4; Untreated, wild-type without CCl_4 treatment).
(**A**) Generation of advanced chronic liver fibrosis/cirrhosis by CCl_4 in mice lacking liver Fn (Fn(f/f)/*Mx-Cre*+). (Upper panels) Western blot analysis of Fn (plasma and cellular types) in liver tissue lysates from control and mutant mice before (0 week) and at 17 weeks of CCl_4 treatment. (Lower panel) Analysis of Fn intensities at 17 weeks of CCl_4 treatment. Fn expression levels are shown relative to the control value of 100 (percent of control). Error bars represent standard deviation (n = 5 for each group). Note that the depletion of Fn in mutant livers is ~98% (**, $P < 0.01$).
(**B**) Analysis of body weight. Data are means ± S.D. ($n = 5$ for each group). Note that both control and mutant body weights show similar patterns during the continuous phase of hepatic damage caused by CCl_4.
(**C**) Serum alanine aminotransferase (ALT) levels and albumin/globulin (A/G) ratio. Data are means ± S.D. ($n = 6$ for each group). Note that while both ALT levels and A/G ratio are gradually decreased in both control and mutant mice, they show similar patterns throughout the process.
(**D**) Upper panels: Mice lacking Fn develop more pronounced liver fibrosis/cirrhosis, as identified by Sirius Red staining at 17 weeks of CCl_4 treatment. Bar = 100 μm. Lower panel: Quantification of fibrosis at 17 weeks of CCl_4 treatment based on Sirius Red staining. Data are means ± S.D. ($n = 5$ for each group). Note that significantly more fibrosis is induced in mutant livers compared to controls (**, $P < 0.01$).

Fig. 2. Significantly elevated myofibroblast activity in Fn-null livers at 17 weeks of CCl_4 treatment.
(**A**) Left panels: Expression of αSMA (in red) shown by immunofluorescence staining at 0 (untreated) and 17 weeks of CCl_4 treatment. Bar = 100 μm. Right panel: Quantification of αSMA positive areas at 17 weeks of CCl_4 treatment (large blood vessel-positive areas [b] shown in left panels were subtracted). Data are means ± S.D. ($n = 4$ in each group; **, $P < 0.01$).
(**B**) Left panel: Western blot analysis of myofibroblast marker αSMA protein expression at 17 weeks of CCl_4 treatment. Right panel: Analysis of αSMA intensities. Band intensity was measured by densitometry and normalized to β-actin (loading control). The αSMA expression levels are shown relative to the control value of 100 (percent of control). Data are means ± S.D. ($n = 3$ for control and 4 for null mice; *, $P < 0.05$).
(**C**) Immunostaining for cleaved caspase 3 (caspase 3 in brown; nuclei in blue). Note that no apparent positive cells are visible. Bar = 25 μm.

Fig. 3. Significant hepatic dysfunction and increased liver-tissue stiffness in Fn-null livers.
(**A**) - (**C**) Serum levels of the hepatic biochemical markers total bilirubin (**A**), cholinesterase (**B**), and albumin (**C**) during chronic liver injury. Data are means ± S.D. ($n = 6$ for each group). Note that considerable loss of hepatic functional reserve is demonstrated in mutant livers, as evidenced by significant upregulation of total bilirubin and downregulation of cholinesterase levels (*, $P < 0.05$; **, $P < 0.01$).
(**D**) - (**G**) Analysis of liver tissue stiffness using AFM at 17 weeks of CCl_4 treatment.
(**D**) Elastic modulus in liver tissues. Data are means ± S.D. Note that elastic modulus are significantly higher in mutant livers (n [measured areas] = 9 for each group *, $P < 0.05$).
(**E**) Gaussian fit of elastic modulus distribution determined pixel-by-pixel with the Peakforce method in a typical collagen fibril-rich area in each group (2 x 2 μm images were used for this analysis).
(**F, G**) AFM images showing (F) a map of mechanical properties (log of the elastic modulus) and (G) topography (height) of collagen fibrils in control and Fn-null liver at 17 weeks of CCl4 treatment. Note that mutant livers show thinner and more dispersed fibrils.

Fig. 4. Lack of Fn results in elevated accumulation of latent TGF-β complexes and continuous activation of TGF-β during chronic liver injury.
(**A**) Significantly increased accumulation of LAP and LTBP-1, -3 and -4 (in red) in the ECM of mutant livers at 17 weeks of CCl_4 treatment shown by immunofluorescence staining using serial sections (**, $P < 0.01$). Bar = 100 μm.

(**B**) Active TGF-β bioassay at 8 and 17 weeks of CCl_4 treatment. Data are means ± S.D. (n = 6 for each group). Note that mutant livers show significantly elevated local TGF-β activity at both time points (*, $P < 0.05$; **, $P < 0.01$).
(**C**) Left panels: Immunostaining for pSmad2/3. Sections were counterstained with hematoxylin. Bar = 25 μm. Right panel: Analysis of pSmad2/3-positive cells. Data are means ± S.D. (n = 10 in each group). Note that the number of nuclear pSmad2/3-positive (in brown) non-parenchymal cells (NPCs; red arrowheads) in mutant livers is significantly higher than controls at 17 weeks of CCl_4 treatment (**, $P < 0.01$). For comparison, hepatocyte nuclei (~two- to three-hold larger than those in non-parenchymal cells) are indicated (black arrows).
(**D**) Left panels: Double immunohistochemical staining for pSmad2/3 (in purple/blue) and αSMA (in brown). Note that the nuclear pSmad2/3-positive cells express myofibroblast marker αSMA in their cytoplasms (black arrowheads). Bar = 25 μm. Right panel: Analysis of pSmad2/3 and αSMA double-positive myofibroblasts. Data are means ± S.D. (n = 10 in each group; **, $P < 0.01$).

Fig. 5. Fn-null livers accumulate more extensive and disorganized collagen fibril networks at 17 weeks of CCl_4 treatment.
(**A**) Upper panels: Deposition of type III and type I collagens at 0 (untreated) and 17 weeks of CCl_4 treatment by immunofluorescent staining. Depositions at 17 weeks are shown using serial sections. Bar = 100 μm. Lower panels: Quantification of positive areas at 17 weeks of CCl_4 treatment. Data are means ± S.D. (n = 4 for each group). Note that deposition of type III and type I collagen is significantly increased in mutant livers compared to controls at 17 weeks of CCl_4 treatment (**, $P < 0.01$).
(**B**) Real-time PCR analysis of *Col1a1* mRNA levels. Relative mRNA expression levels are shown relative to the control value of 1. Data are means ± S.D. (n = 5 for each group). Note that collagen mRNA levels in mutant livers are significantly upregulated (*, $P < 0.05$).
(**C**) - (**E**) Analysis of assembled fibrils using polarized microscopy.
(**C**) Immunofluorescent staining for type I collagen (first upper 2 panels), and representative images of retardance and orientation by Sirius Red-stained serial sections (second and third 2 panels, respectively). The level of retardation is denoted by a pixel color, as indicated by the color legend (from purple [the lowest] to red [the highest]). Note that the maximum magnitude of retardance (red color) is identical in the control and mutant liver. Bars = 25 μm.
(**D**) Representative distribution patterns of fibril bundle orientation in the control and mutant livers. The x-axis represents the orientation angle. This is divided into 10° increments and 0° corresponds to the mean orientation of distributions. The y-axis shows the percentage of fibril bundles within 10° orientation angle range. Note that orientation of fibril bundles in mutant livers is less aligned and more disorganized compared to controls. AD, angular deviation.
(**E**) The average angular deviation of orientation distributions. Data are means ± S.D. Note that angular deviation is significantly larger in mutant livers (**, $P < 0.01$).
(**F**) Real-time PCR analysis of *MMP8 and MMP13* mRNA levels. Relative mRNA expression levels are shown relative to the control value of 1. Data are means ± S.D. (n = 5 for each group). Note that the expression levels are not significantly different.

Fig. 6. Contribution of type V collagen to advanced chronic liver injury and collagen fibril ultrastructure at 17 weeks of CCl_4 treatment.
(**A**) Significantly increased deposition and assembly of type V collagen in mutant livers shown by immunofluorescence staining using serial sections (type V collagen in green; type I collagen in red; Fn in red; DAPI [cell nuclei] in blue) (n = 4 for each group; **, $P < 0.01$). Bar = 50 μm.
(**B**) Real-time PCR analysis of *Col5a1* mRNA levels. Relative mRNA expression levels are shown relative to the control value of 1.0. Data are means ± S.D. (n = 4 for each group). Note that expression levels in mutant livers are ~1.5-fold increased but not significantly different.
(**C**) - (**F**) Ultrastructural analysis of collagen fibrils using TEM.
(**C**) Electron micrographs of longitudinal (upper panel) and transverse (lower panel) sections. Bar = 100 nm.
(**D**) Left panel: The average diameter of collagen fibrils (1,500 fibrils for each group: 375 fibrils per animal, n = 4, were calculated). Note that the average fibril diameter is identical between control and mutant livers. Right panel: Morphometric analysis of collagen fibril diameter (1,500 fibrils for each group: 375 fibrils per animal, n = 4, were

calculated). Note the ~33% increase in the thinner (30-40 nm diameter) and the ~21% decrease in the number of thicker (50-60 nm diameter) collagen fibril-subpopulations evident in mutant livers.
(**E**) Collagen fibril number. Data are means ± S.D. Note that the fibril number is significantly higher in mutant livers (n [measured areas] = 18 for each group **, $P < 0.01$).
(**F**) Hydroxyproline contents. Data are means ± S.D. ($n = 4$ for each group). Note that net hepatic collagen content in mutant livers is significantly increased (*, $P < 0.05$).

Fig. 7. Elevated LOX expression level in Fn-null liver at 17 weeks of CCl_4 treatment and its mechanism.
(**A**) Real-time PCR analysis of *LOX and LOXL1-4* mRNA levels in control and mutant livers. Relative mRNA expression levels are shown relative to the control value of 1. Error bars represent standard deviation ($n = 4$ for each group; *, $P < 0.05$; **, $P < 0.01$).
(**B**) Left panels: Western blot analysis of LOX in Fn-null and its parental hepatic stellate cell (HSC) lines with or without treatment of 2 pM TGF-β1 *in vitro*. Aorta tissue lysates from adult wild-type mice were used as a positive control. Right panel: Analysis of induction levels of active LOX in response to TGF-β1 (fold increase). Band intensity was measured by densitometry and normalized to HSC70 (loading control). Data are from three independent experiments. **, $P < 0.01$.
(**C**) Left Panels: Double immunofluorescence staining for LOX (in green) and DAPI (in blue) in Fn-null hepatic stellate cells (HSC) cultured for 18 h with or without 2 pM TGF-β1 treatment. Bar = 25 μm. Right panel: The effect of Smad3 inhibitor SIS3, PI3-kinase inhibitor LY294002, p38 MAP kinase inhibitor PD169316, JNK inhibitor 420119, and MEK1/2 inhibitor PD98059 on TGF-β1 induced LOX expression in Fn-null hepatic stellate cells. Data are means ± S.D. **, $P < 0.01$.

Fig. 8. Structural and mechanical integrity of formed collagen fibril networks in Fn-null hepatic stellate cells.
(**A**) Elastic modulus of collagen fibrils in Fn-null hepatic stellate cells without treatment (Ntx) or with TGF-β1 or TGF-β1 plus 200 μM BAPN, and parental (control) cells without treatment cultured for 7 days. Data are means ± S.D. (n [measured areas] = 7 for Fn-null cells; 6 for parental cells. **, $P < 0.01$). #, Fn-null stellate cells do not form collagen fibril network in culture without treatment (26).
(**B**) Immunofluorescence staining for type I collagen (in red) (upper panels) and images showing a peak force error by AFM (lower panels) in Fn-null hepatic stellate cells (HSC) cultured for 7 days with TGF-β1 or TGF-β1 plus 200 μM BAPN. Bar in fluorescence staining = 25 μm. Note that BAPN treatment results in the disruption of longitudinal collagen bundle formation.
(**C**) Elastic modulus of collagen fibrils in Fn-null hepatic stellate cells with 10 μg/ml plasma Fn and parental (control) cells cultured for 7 days. Data are means ± S.D. (n [measured areas] = 6 for each group). n.s., not significantly different.

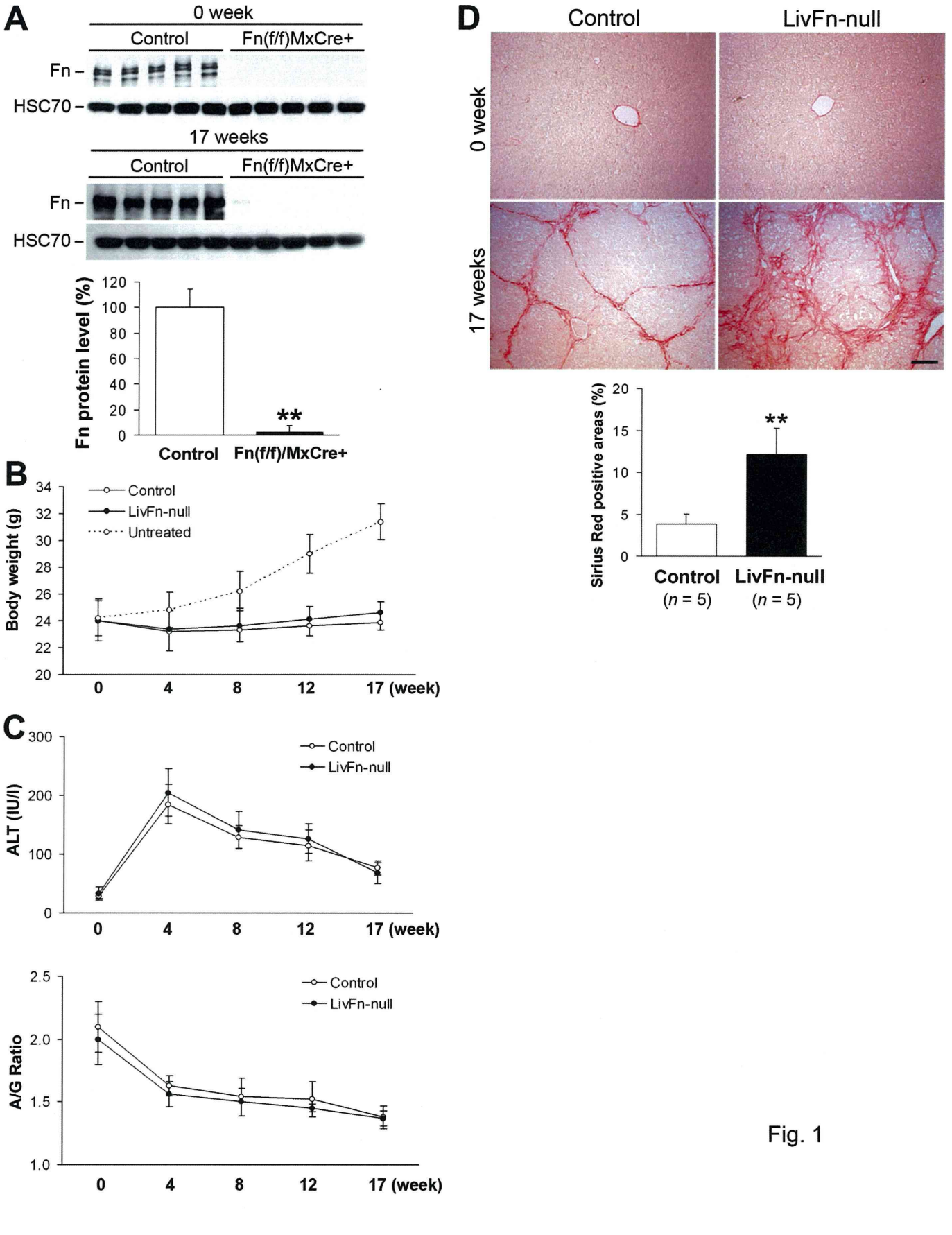
A
0 week
Control
Fn(f/f)MxCre+
Fn –
HSC70 –
17 weeks
Control
Fn(f/f)MxCre+
Fn –
HSC70 –
Fn protein level (%)
120
100
80
60
40
20
0
**
Control
Fn(f/f)/MxCre+
B
Body weight (g)
34
32
30
28
26
24
22
20
Control
LivFn-null
Untreated
0
4
8
12
17 (week)
C
ALT (IU/l)
300
200
100
0
Control
LivFn-null
0
4
8
12
17 (week)
A/G Ratio
2.5
2.0
1.5
1.0
Control
LivFn-null
0
4
8
12
17 (week)
D
Control
LivFn-null
0 week
17 weeks
Sirius Red positive areas (%)
20
15
10
5
0
**
Control
(n = 5)
LivFn-null
(n = 5)

Fig. 1

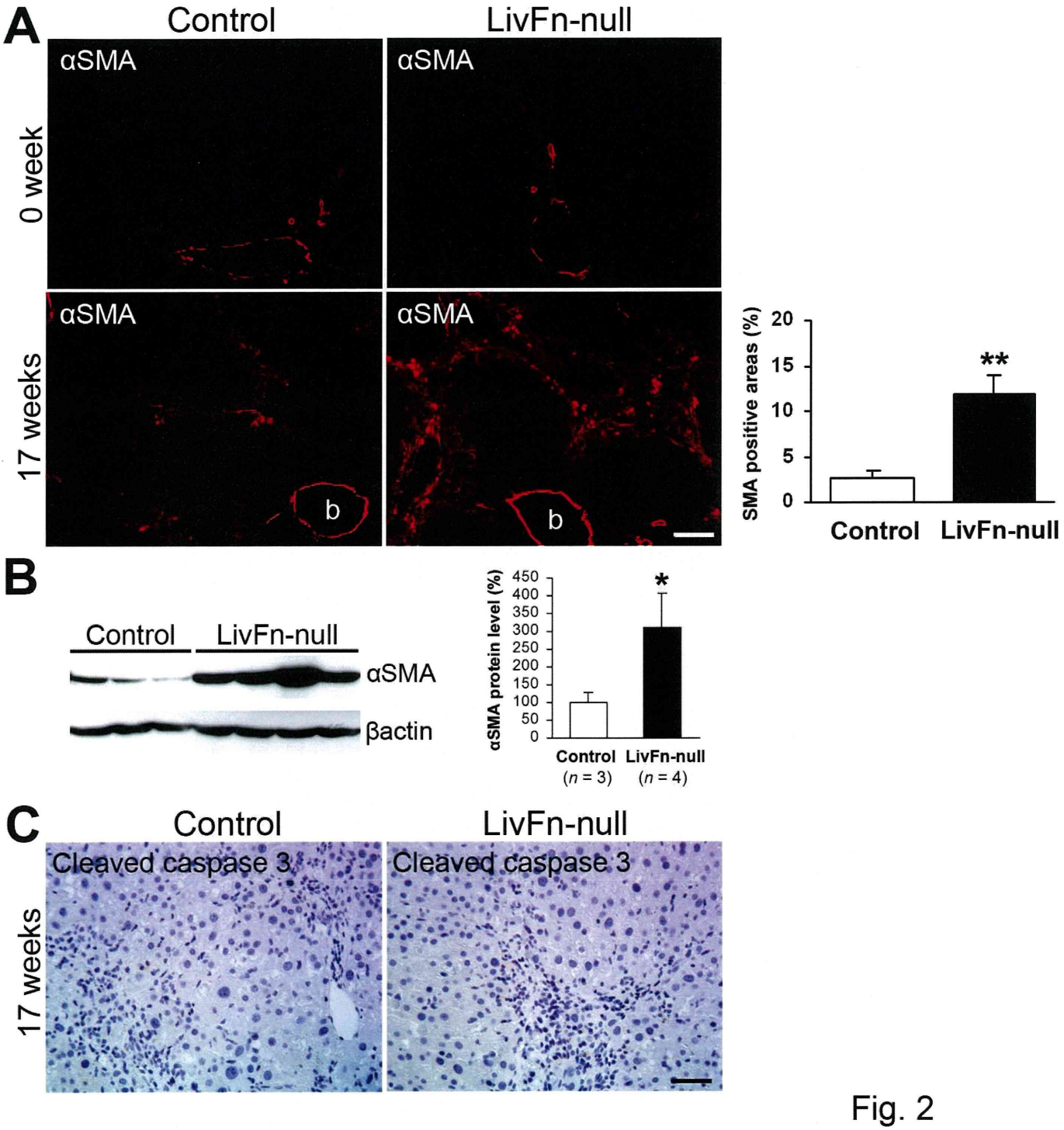
A
Control
LivFn-null
αSMA
αSMA
0 week
αSMA
αSMA
17 weeks
b
b
SMA positive areas (%)
20
15
10
5
0
**
Control
LivFn-null
B
Control
LivFn-null
αSMA
βactin
αSMA protein level (%)
450
400
350
300
250
200
150
100
50
0
*
Control
(n = 3)
LivFn-null
(n = 4)
C
Control
LivFn-null
Cleaved caspase 3
Cleaved caspase 3
17 weeks

Fig. 2

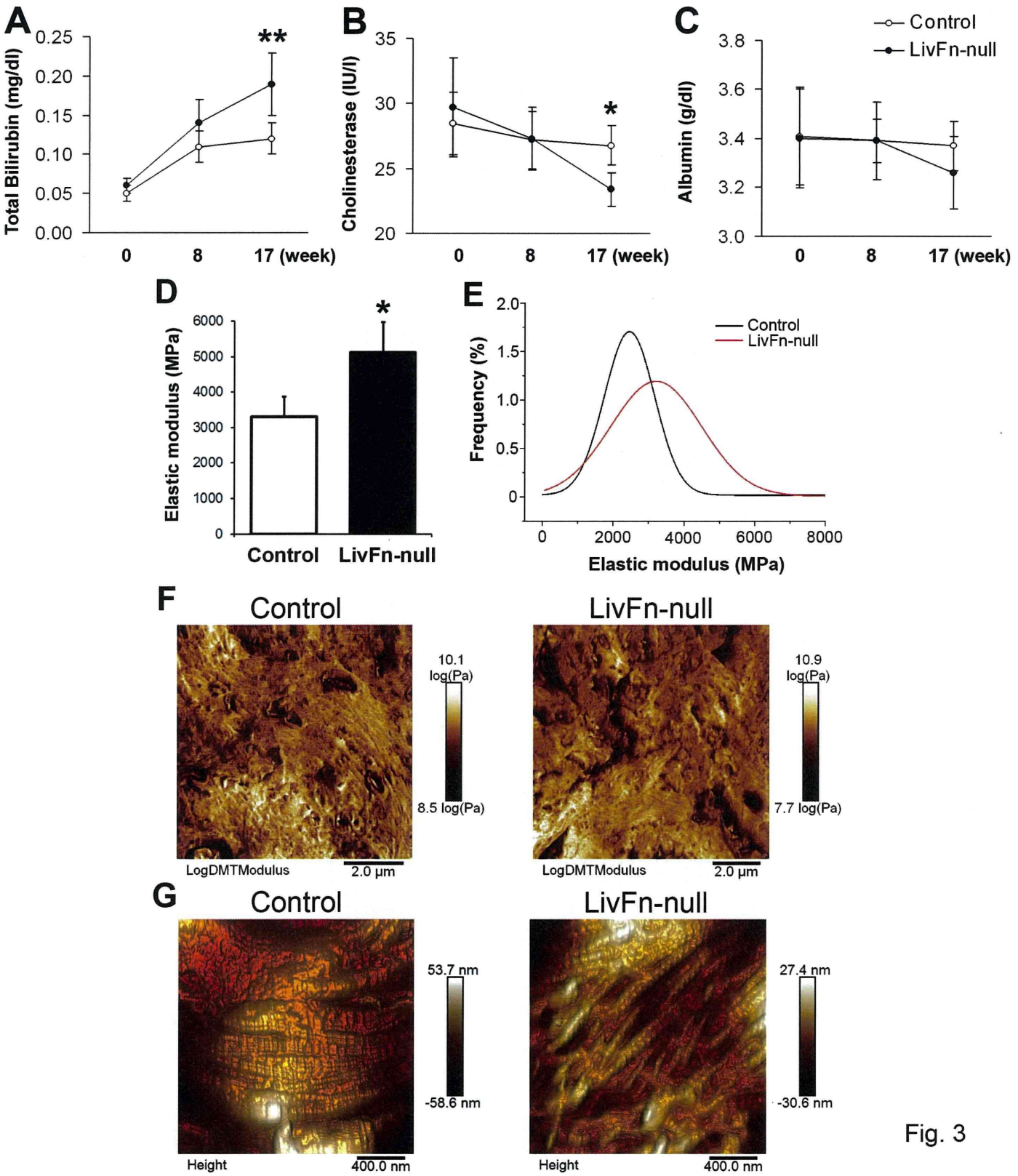
A
Total Bilirubin (mg/dl)
0.25
0.20
0.15
0.10
0.05
0.00
**
0
8
17 (week)
B
Cholinesterase (IU/l)
35
30
25
20
*
0
8
17 (week)
C
Albumin (g/dl)
3.8
3.6
3.4
3.2
3.0
Control
LivFn-null
0
8
17 (week)
D
Elastic modulus (MPa)
6000
5000
4000
3000
2000
1000
0
*
Control
LivFn-null
E
Frequency (%)
2.0
1.5
1.0
0.5
0
Control
LivFn-null
0
2000
4000
6000
8000
Elastic modulus (MPa)
F
Control
10.1
log(Pa)
8.5 log(Pa)
LogDMTModulus
2.0 µm
LivFn-null
10.9
log(Pa)
7.7 log(Pa)
LogDMTModulus
2.0 µm
G
Control
53.7 nm
-58.6 nm
Height
400.0 nm
LivFn-null
27.4 nm
-30.6 nm
Height
400.0 nm

Fig. 3

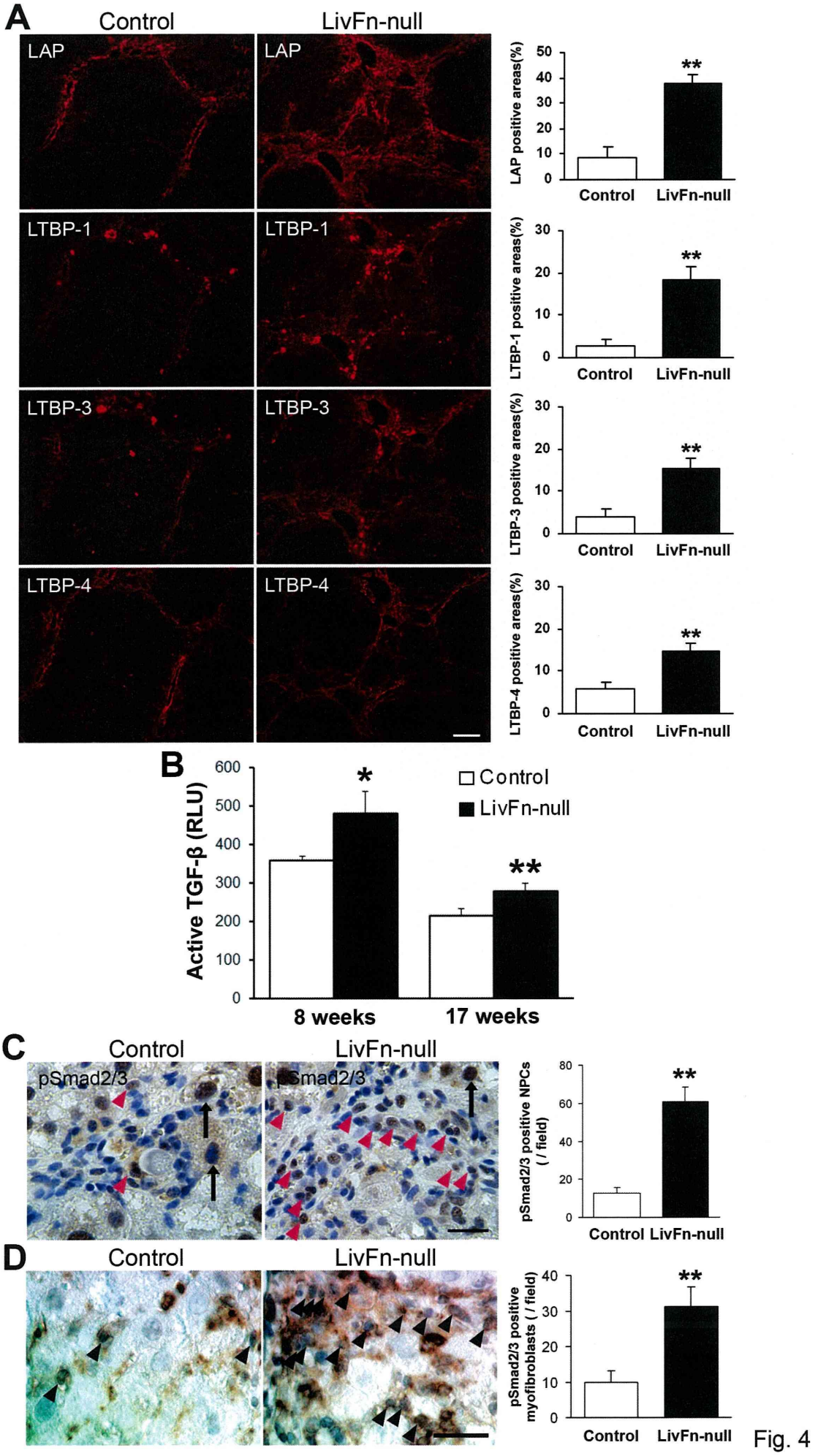
A
Control
LivFn-null
LAP
LTBP-1
LTBP-3
LTBP-4
LAP positive areas(%)
LTBP-1 positive areas(%)
LTBP-3 positive areas(%)
LTBP-4 positive areas(%)
Control
LivFn-null
B
Active TGF-β (RLU)
Control
LivFn-null
8 weeks
17 weeks
C
pSmad2/3
pSmad2/3 positive NPCs (/ field)
D
pSmad2/3 positive myofibroblasts (/ field)

Fig. 4

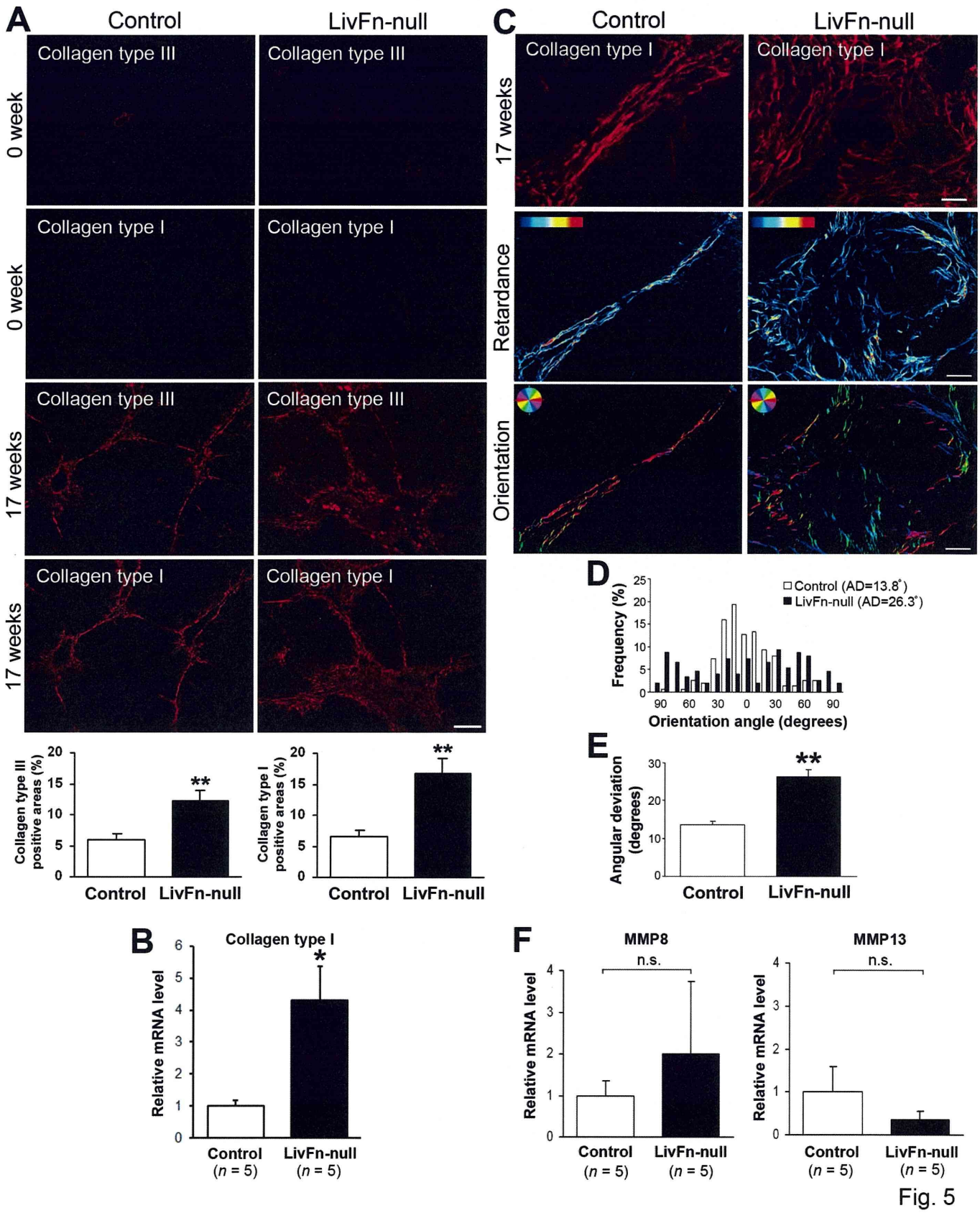
A
Control
LivFn-null
Collagen type III
Collagen type I
0 week
17 weeks
Collagen type III positive areas (%)
Collagen type I positive areas (%)
**
Control
LivFn-null
B
Collagen type I
Relative mRNA level
*
Control (n = 5)
LivFn-null (n = 5)
C
Retardance
Orientation
D
Frequency (%)
Control (AD=13.8°)
LivFn-null (AD=26.3°)
Orientation angle (degrees)
E
Angular deviation (degrees)
F
MMP8
MMP13
n.s.

Fig. 5

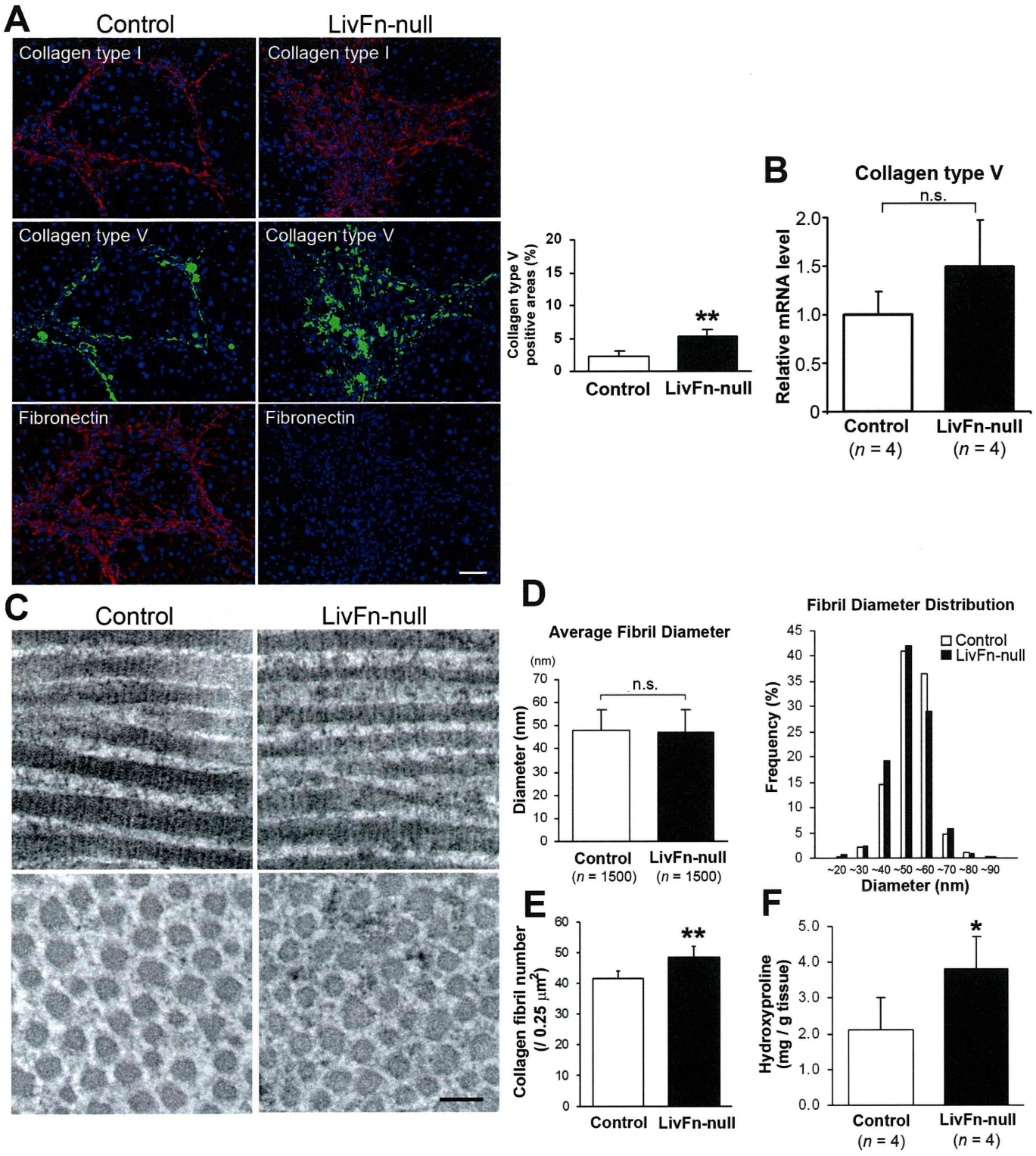
A
Control
LivFn-null
Collagen type I
Collagen type I
Collagen type V
Collagen type V
Fibronectin
Fibronectin
Collagen type V positive areas (%)
20
15
10
5
0
**
Control
LivFn-null
B
Collagen type V
n.s.
Relative mRNA level
2.0
1.5
1.0
0.5
0
Control
(n = 4)
LivFn-null
(n = 4)
C
Control
LivFn-null
D
Average Fibril Diameter
(nm)
70
60
50
40
30
20
10
0
n.s.
Diameter (nm)
Control
(n = 1500)
LivFn-null
(n = 1500)
Fibril Diameter Distribution
Control
LivFn-null
Frequency (%)
45
40
35
30
25
20
15
10
5
0
~20 ~30 ~40 ~50 ~60 ~70 ~80 ~90
Diameter (nm)
E
Collagen fibril number
(/ 0.25 μm²)
60
50
40
30
20
10
0
**
Control
LivFn-null
F
Hydroxyproline
(mg / g tissue)
5.0
4.0
3.0
2.0
1.0
0.0
*
Control
(n = 4)
LivFn-null
(n = 4)

Fig. 6

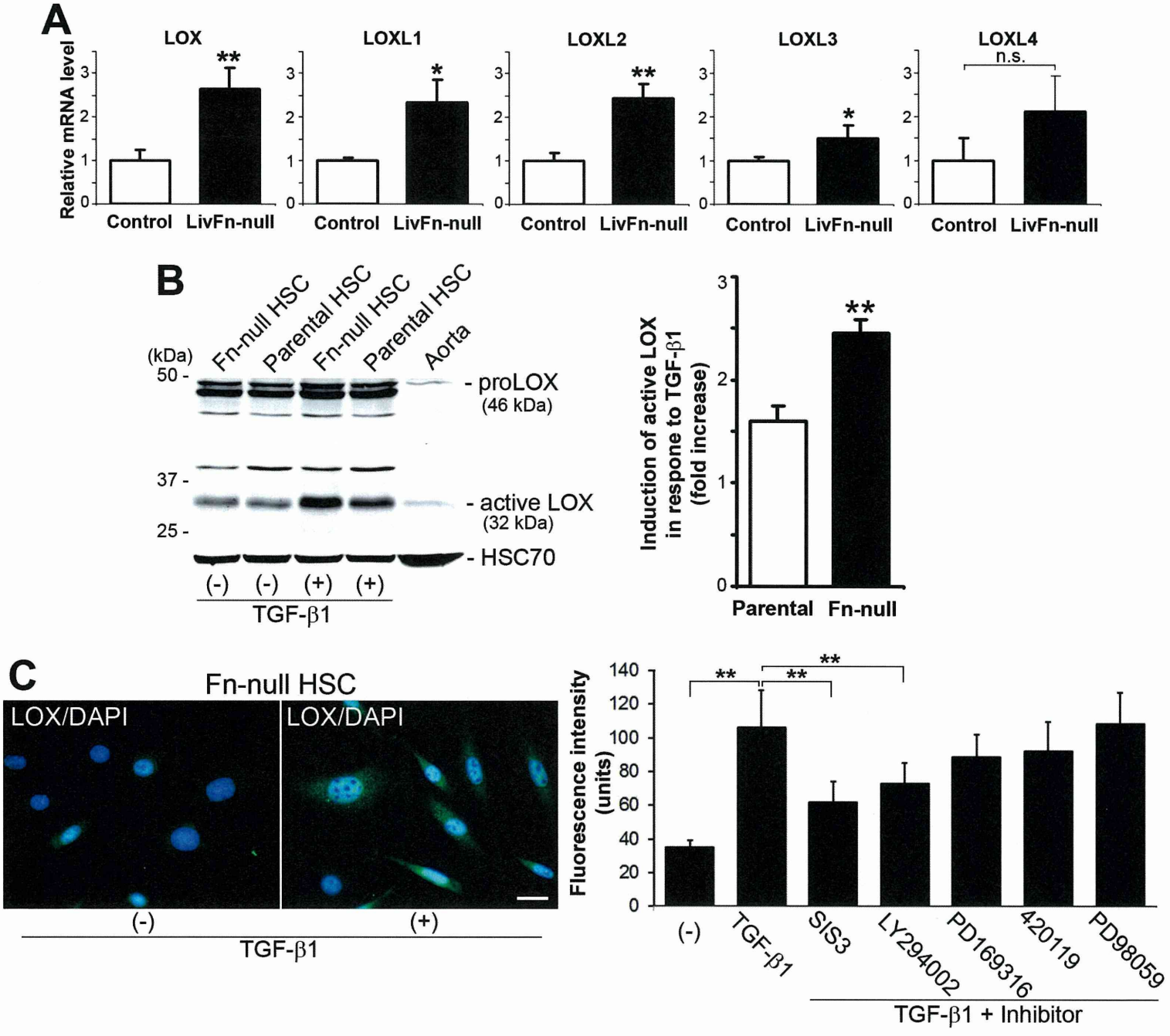
A
LOX
LOXL1
LOXL2
LOXL3
LOXL4
n.s.
Relative mRNA level
Control
LivFn-null
B
Fn-null HSC
Parental HSC
Fn-null HSC
Parental HSC
Aorta
(kDa)
50 -
37 -
25 -
- proLOX
(46 kDa)
- active LOX
(32 kDa)
- HSC70
(-) (-) (+) (+)
TGF-β1
Induction of active LOX in respone to TGF-β1 (fold increase)
Parental
Fn-null
C
Fn-null HSC
LOX/DAPI
LOX/DAPI
(-)
(+)
TGF-β1
Fluorescence intensity (units)
(-)
TGF-β1
SIS3
LY294002
PD169316
420119
PD98059
TGF-β1 + Inhibitor

Fig. 7

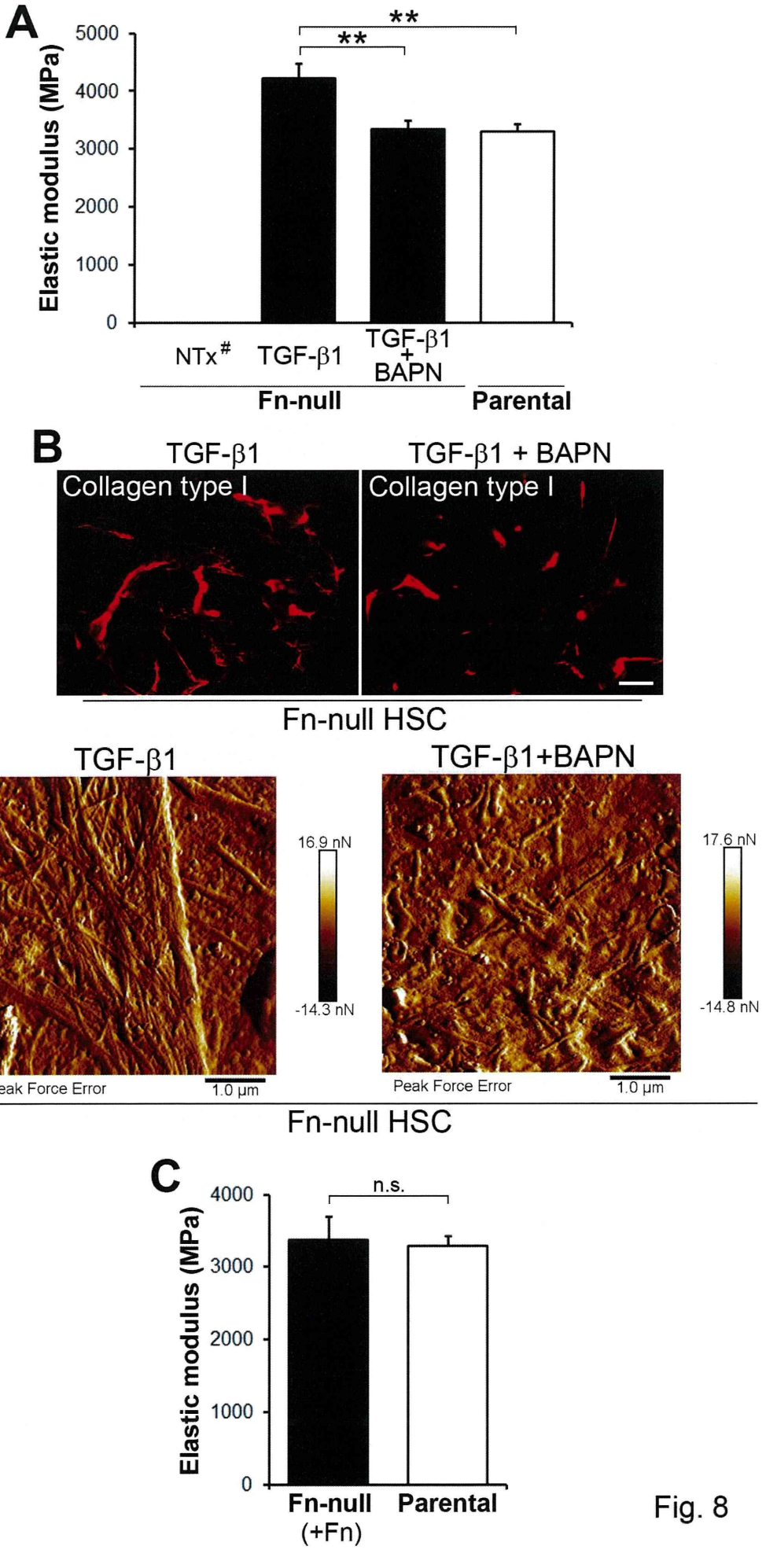
A
Elastic modulus (MPa)
5000
4000
3000
2000
1000
0
**
**
NTx#
TGF-β1
TGF-β1 + BAPN
Fn-null
Parental
B
TGF-β1
TGF-β1 + BAPN
Collagen type I
Collagen type I
Fn-null HSC
TGF-β1
TGF-β1+BAPN
16.9 nN
-14.3 nN
17.6 nN
-14.8 nN
Peak Force Error
1.0 μm
Peak Force Error
1.0 μm
Fn-null HSC
C
Elastic modulus (MPa)
4000
3000
2000
1000
0
n.s.
Fn-null (+Fn)
Parental

Fig. 8

JOURNAL OF APPLIED PHYSICS 117, 17D157 (2015)

Alternating current magnetic susceptibility and heat dissipation by $Mn_{1-x}Zn_xFe_2O_4$ nanoparticles for hyperthermia treatment

T. Kondo,[1] K. Mori,[1] M. Hachisu,[1] T. Yamazaki,[1] D. Okamoto,[2] M. Watanabe,[2] K. Gonda,[3,4] H. Tada,[5] Y. Hamada,[4] M. Takano,[4] N. Ohuchi,[4,5] and Y. Ichiyanagi[1,a)]
[1]*Department of Physics, Graduate School of Engineering, Yokohama National University, Yokohama 240-8501, Japan*
[2]*Department of Materials Science and Chemical Engineering, Graduate School of Engineering, Yokohama National University, Yokohama 240-8501, Japan*
[3]*Department of Medical Physics, Graduate School of Medicine, Tohoku University, Sendai 980-8575, Japan*
[4]*Department of Nano-Medical Science, Graduate School of Medicine, Tohoku University, Sendai 980-8575, Japan*
[5]*Department of Surgical Oncology, Graduate School of Medicine, Tohoku University, Sendai 980-8575, Japan*

(Presented 6 November 2014; received 23 September 2014; accepted 6 November 2014; published online 4 May 2015)

Mn-Zn ferrite, $Mn_{1-x}Zn_xFe_2O_4$ nanoparticles encapsulated in amorphous SiO_2 were prepared using our original wet chemical method. X-ray diffraction patterns confirmed that the diameters of these particles were within 7–30 nm. Magnetization measurements for various sample compositions revealed that the saturation magnetization (M_s) of 7 nm particles was maximum for the $x = 0.2$ sample. AC magnetic susceptibility measurements were performed for $Mn_{0.8}Zn_{0.2}Fe_2O_4$ ($x = 0.2$) samples with 13–30 nm particles. The peak of the imaginary part of the magnetic susceptibility χ'' shifted to higher temperatures as the particle size increased. An AC field was found to cause the increase in temperature, with the 18 nm particles exhibiting the highest temperature increase, as expected. In addition, *in vitro* experiments were carried out to study the hyperthermia effects of $Mn_{1-x}Zn_xFe_2O_4$ ($x = 0.2$, 18 nm) particles on human cancer cells. © *2015 AIP Publishing LLC*.
[http://dx.doi.org/10.1063/1.4919327]

I. INTRODUCTION

Recently, magnetic nanoparticles have attracted attention because of their potential medical applications such as in MRI contrast agents, drug delivery systems (DDS), and hyperthermia treatments.[1–9] We have reported on the magnetic properties of various iron oxides and suggested the possibility of magnetic nanoparticles for biomedical applications.[10–12] Some reports have found the doping effect in iron oxide, and magnetic parameters, such as permeability or saturation magnetization, were improved by doping with B_2O_3, Co, or Zn ions.[13,14]

In this report, Zn-doped $MnFe_2O_4$ nanoparticles were prepared, Zn content was varied, and composition dependence was first examined by dc and ac magnetization measurements. Based on the results, heating efficiency was obtained for magnetic hyperthermia treatments. Finally, *in vitro* experiments were performed for human cancer cells, and the hyperthermia effects of the nanoparticles were evaluated.

II. EXPERIMENT

$Mn_{1-x}Zn_xFe_2O_4$ ($x = 0$, 0.1, 0.2, 0.3, 0.4, 0.5, 0.6, 0.7, 0.8) nanoparticles were prepared by a wet chemical method. Aqueous solutions of $MnCl_2{\cdot}4H_2O$, $ZnCl_2$, and $FeCl_2{\cdot}4H_2O$ were mixed with a solution of $Na_2SiO_3{\cdot}9H_2O$. The mole ratio of the prepared reagent was Mn:Zn:Fe:Si = 1−*x*:*x*:2:3. The precipitates were washed several times with distilled water and dried at about 350 K in a thermostat. The as-prepared samples were then subjected to heat treatment in a furnace with an Ar environment. Particle sizes were controlled by setting the annealing temperature. All samples were examined by Cu$K\alpha$ X-ray powder diffraction ($\lambda = 0.154$ nm) and X-ray fluorescence analyses. DC magnetization of the samples was measured using a SQUID magnetometer in a ±50 kOe magnetic field at 300 K. The AC magnetic susceptibility of the samples was measured under a 1 Oe, 100 Hz alternating magnetic field. The temperature increase of these particles was measured under a 62–151 Oe, 15 kHz alternating magnetic field. The *in vitro* experiments were performed under a 90 Oe, 31 kHz alternating magnetic field at 310 K. Human prostate cancer cells (DU145) and human breast cancer cells (KPL4, MCF7, MDA-MB231) were cultured in a dish and exposed to an AC field.

III. RESULTS AND DISCUSSION

A. X-ray diffraction (XRD) and X-ray fluorescence analyses

Fig. 1 shows the XRD patterns for $Mn_{1-x}Zn_xFe_2O_4$ ($x = 0$, 0.1, 0.2, 0.3, 0.5, 0.7, 0.9, 1) samples. A single-phase spinel structure was observed with broad peaks of $2\theta \sim 20°$, because of amorphous SiO_2, and the particle size was estimated by crystal size distribution analysis (CSDA). The samples prepared using this method consisted of magnetic clusters encapsulated by amorphous SiO_2. The average particle sizes of all samples were controlled to be approximately 7 nm by setting the annealing temperature. Results of X-ray fluorescence analysis showed that Zn^{2+} ions were doped

a)Author to whom correspondence should be addressed. Electronic mail: yuko@ynu.ac.jp.

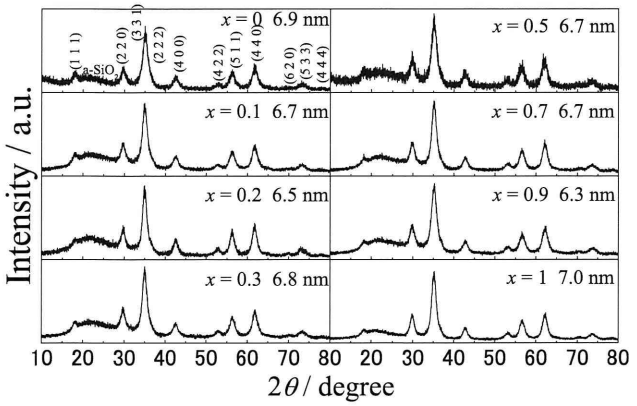

FIG. 1. X-ray diffraction patterns of $Mn_{1-x}Zn_xFe_2O_4$ ($x = 0$, 0.1, 0.2, 0.3, 0.5, 0.7, 0.9, 1) for particle sizes of 7 nm.

appropriately since the doping ratio increased consistently with our preparation rate.

B. DC magnetization measurements

Fig. 2 shows the magnetization curves for $Mn_{1-x}Zn_xFe_2O_4$. The samples were measured at 300 K under a ±50 kOe field. Fig. 3 shows the maximum magnetization of each composition. The M_s was largest at $x = 0.2$. This phenomenon could be explained as follows. On doping, Zn^{2+} ions prefer to distribute at the A-sites, causing an increase in magnetic ions at the B-sites. The difference in magnetic moments of the A- and B-sites causes a net increase in magnetization of the material.[15] Uncompensated magnetic spins exist on the surface of the small particles, and the anisotropy energy would be equivalent to the thermal energy for the definite composition at the observed temperature of 310 K. The larger the maximum magnetization, the higher the heating efficiency, as seen from (1). Hence, the $x = 0.2$ is expected to have high heating efficiency. Different particle sizes of the $x = 0.2$ samples were prepared in order to determine the optimum particle size.

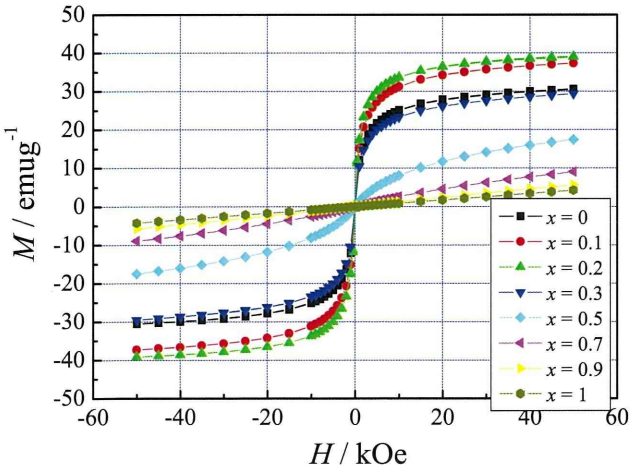

FIG. 2. Magnetization curves of $Mn_{1-x}Zn_xFe_2O_4$ (x = 0, 0.1, 0.2, 0.3, 0.5, 0.7, 0.9, 1) for particle sizes of 7 nm.

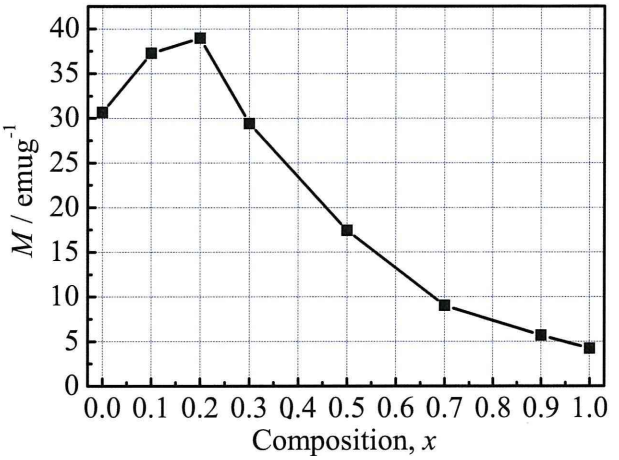

FIG. 3. *M*s of $Mn_{1-x}Zn_xFe_2O_4$ ($x = 0$, 0.1, 0.2, 0.3, 0.5, 0.7, 0.9, 1) for particle sizes of 7 nm.

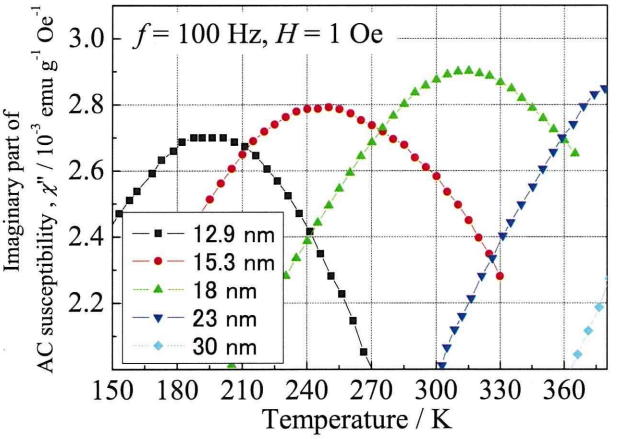

FIG. 4. Imaginary part of the AC magnetic susceptibility of $Mn_{1-x}Zn_xFe_2O_4$ ($x = 0.2$) for various particle sizes.

C. AC magnetic susceptibility

In order to estimate heat dissipation, AC magnetic susceptibility was measured. We prepared superparamagnetic nanoparticles so that the system could exhibit Néel relaxation.

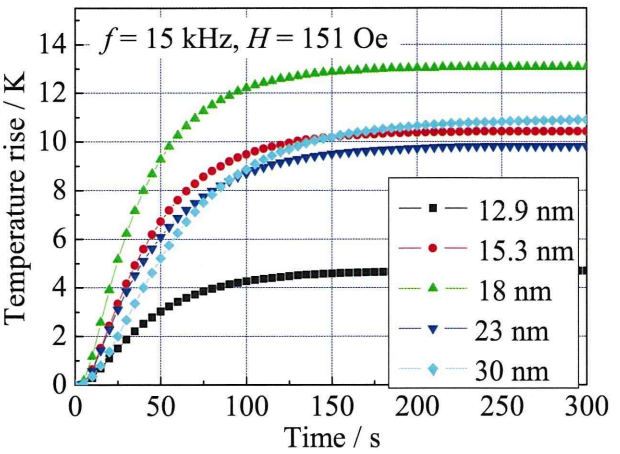

FIG. 5. Temperature rise of the samples in the AC magnetic field of $Mn_{1-x}Zn_xFe_2O_4$ ($x = 0.2$) for various particle sizes.

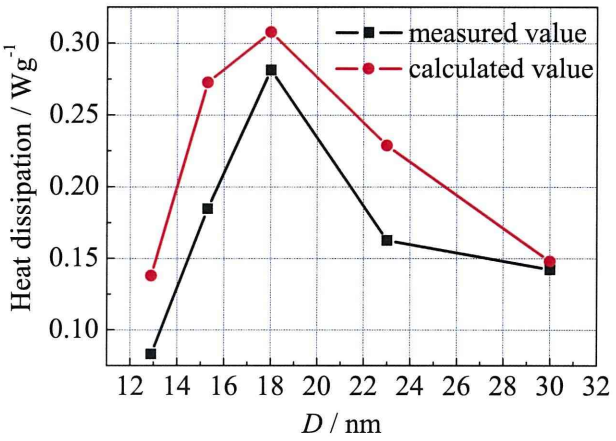

FIG. 6. Comparison of calculated value and measured value of the heat dissipation versus particle size.

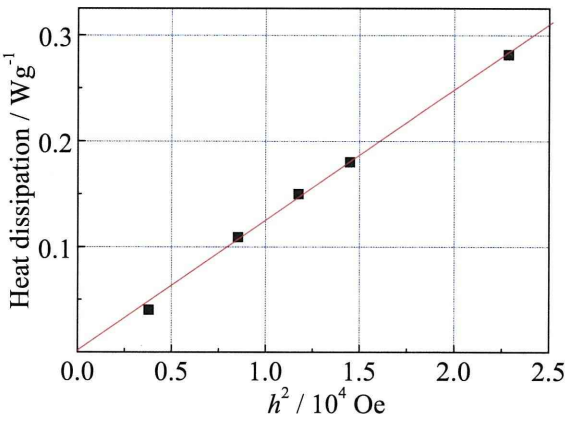

FIG. 7. Magnetic field dependence of heat dissipation for the sample of 18 nm.

In Néel relaxation, heat dissipation from the magnetic relaxation loss can be expressed by the following equation:[15–17]

$$P = \mu_0 \pi \chi'' f h^2, \quad (1)$$

where μ_0 is the permeability in vacuum, χ'' is the imaginary part of the magnetic susceptibility, f is the frequency of the applied AC magnetic field, and h is the strength of the applied AC magnetic field.

Fig. 4 shows the measurements of the imaginary part of the AC magnetic susceptibility χ,$''$ measured under a 1 Oe, 100 Hz AC magnetic field, for different particle sizes of $Mn_{1-x}Zn_xFe_2O_4$ ($x = 0.2$). Particle sizes were controlled to be between 12.9 nm and 30 nm, depending on the annealing temperature between 1123 K and 1223 K. No morphological change was previously found for particles of these sizes.[11] It is assumed that an acceptable biological temperature is 310 K, and heat dissipation can be predicted for this temperature. Hence, the heating mechanism by magnetic relaxation loss is most efficient for the sample with 18 nm particles.

D. Temperature measurement

Fig. 5 shows the increase in temperature of the samples as a function of time. The temperature was measured after placing the samples in a 151 Oe, 15 kHz AC magnetic field at 310 K. Fig. 6 shows the calculated and measured values of heat dissipation depending on the particle size. A correlation can be observed between the calculated and measured values, suggestive of a magnetic relaxation loss. Further, Fig. 7 shows the magnetic field dependence of heat dissipation for the sample with 18 nm particles. We observe that heat dissipation is proportional to h^2, and from Eq. (1), the heating mechanism is confirmed to be magnetic relaxation loss. Our results confirm that the sample with 18 nm particles has the

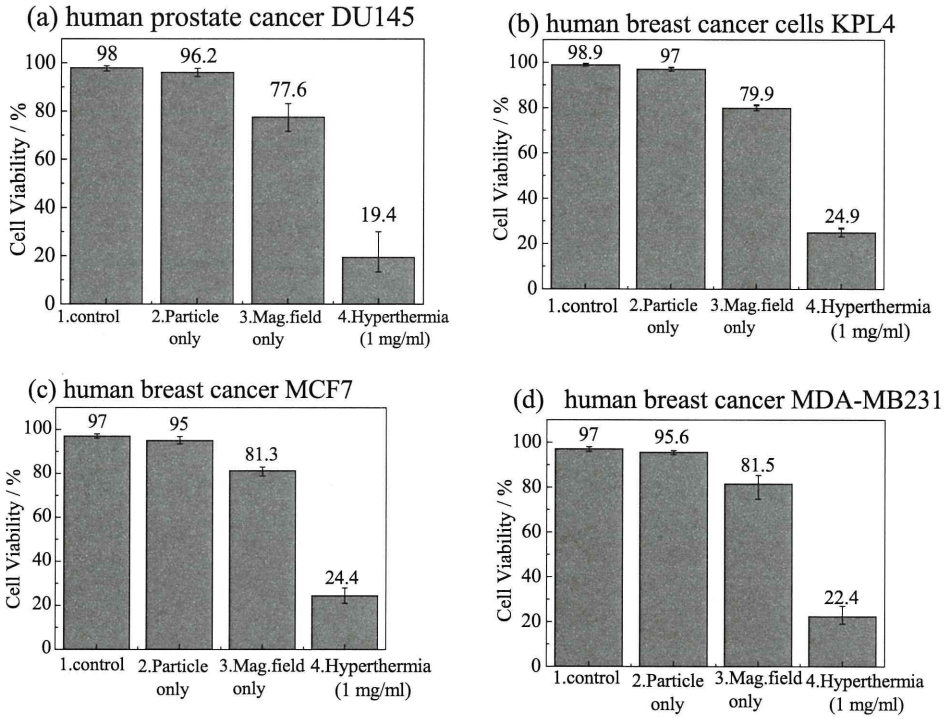

FIG. 8. Cell viability of (a) the human prostate cancer DU145, (b) the human breast cancer KPL4, (c) the human breast cancer MCF7, and (d) human breast cancer cells MDA-MB231.

highest heating efficiency and magnetic relaxation loss. This sample was used for the *in vitro* experiments.

E. *In vitro* experiment results

Human prostate cancer cells (DU145) and breast cancer cells (KPL4, MCF7, MDA-MB231) were cultured in a dish and exposed to an AC magnetic field. The diameter of the coil was changed to ensure that the 35 mm dish fit in the equipment. After the cells were cultured for 24 h, magnetic particles with a concentration of 1 mg/ml were distributed. After application of an AC magnetic field of 31 kHz and 90 Oe for 30 min, the cells were stained with trypan blue, and the remaining cells were counted. Conditions were 1. Control, 2. Particle only, 3. Magnetic field only, and 4. Magnetic Hyperthermia. Fig. 8 shows (a) the human prostate cancer DU145, (b) human breast cancer cells KPL4, (c) human breast cancer MCF7, and (d) human breast cancer MDA-MB231 cells. Results of the "2. Particle only" condition confirm the low toxicity of this sample. Ferrites are generally not considered to be biocompatible; however, our particles showed superior biocompatibility. This fact would be due to the characteristic configuration of the nanoparticles encapsulated with amorphous SiO_2, and this nontoxicity was already confirmed in the previous experiments. Results of the "4. Magnetic Hyperthermia" condition confirmed that most cancer cells are destroyed. The results for different cancer cells under this condition are similar. A decrease in the cell viability of about 80% was observed for all four types of cancer cells, thus confirming that our sample is an effective agent of hyperthermia treatment.

ACKNOWLEDGMENTS

This study was partially supported by a Grand-in Aid for Science Research (No. 23656013) from the Japan Society for the Promotion of Science (JSPS), a grant from the Magnetic Health Science Foundation (2012), and A3 Foresight Program from JSPS (2013).

[1]A. Jordan, R. Scholz, P. Wust, H. Fähling, and R. Felix, J. Magn. Magn. Mater. **201**, 413–419 (1999).
[2]M. Suto, Y. Hirota, H. Mamiya, A. Fujita, R. Kasuya, K. Tohji, and B. Jeyadevan, J. Magn. Magn. Mater. **321**, 1493–1496 (2009).
[3]S. Laurent, S. Dutz, U. O. Häfeli, and M. Mahmoudi, Adv. Colloid Interface Sci. **166**, 8–23 (2011).
[4]T. C. Lin, F. H. Lin, and J. C. Lin, Acta Biomater. **8**, 2704–2711 (2012).
[5]A. Ito, M. Shinkai, H. Honda, and T. Kobayashi, J. Biosci. Bioeng. **100**, 1–11 (2005).
[6]B. Feng, R. Y. Hong, L. S. Wang, L. Guo, H. Z. Li, J. Ding, Y. Zheng, and D. G. Wei, Colloids Surf., A **328**, 52–59 (2008).
[7]Z. Li, M. Kawashita, N. Araki, M. Mitsumori, M. Hiraoka, and M. Doi, Mater. Sci. Eng., C **30**, 990–996 (2010).
[8]A. E. Deatsch and B. A. Evans, J. Magn. Magn. Mater. **354**, 163–172 (2014).
[9]Y. Ichiyanagi, D. Shigeoka, T. Hiroki, T. Mashino, S. Kimura, A. Tomitaka, K. Ueda, and Y. Takemura, Thermochim. Acta **532**, 123–126 (2012).
[10]Y. Ichiyanagi and T. Uehashi, Phys. Status Solidi C **1**, 3485 (2004).
[11]Y. Moro, H. Katayanagi, S. Kimura, D. Shigeoka, T. Hiroki, T. Mashino, and Y. Ichiyanagi, Surf. Interface Anal. **42**, 1655–1658 (2010).
[12]Y. Ichiyanagi, S. Moritake, S. Taira, and M. Setou, J. Magn. Magn. Mater. **310**, 2877–2879 (2007).
[13]P. M. Botta, P. G. Bercoff, E. F. Aglietti, H. R. Bertorello, and J. M. Porto López, Ceram. Int. **32**, 857–863 (2006).
[14]H. Shokrollahi, J. Magn. Magn. Mater. **320**, 463–474 (2008).
[15]E. W. Gorter, Philips Res. Rep. **9**, 295 (1954).
[16]T. Atumi, B. Jeyadevan, Y. Sato, and K. Tohji, J. Magn. Soc. Jpn. **30**, 555–560 (2006).
[17]R. E. Rosensweig, J. Magn. Magn. Mater. **252**, 370–374 (2002).

Adipocyte-Derived Monocyte Chemotactic Protein-1 (MCP-1) Promotes Prostate Cancer Progression Through the Induction of MMP-2 Activity

Yusuke Ito,[1] Hitoshi Ishiguro,[1,2] Naohito Kobayashi,[1] Hisashi Hasumi,[1] Masatoshi Watanabe,[3] Masahiro Yao,[1] and Hiroji Uemura[1]*

[1]*Department of Urology, Yokohama City University Graduate School of Medicine, Yokohama, Japan*
[2]*Photocatalyst Group, Kanagawa Academy of Science and Technology, Kawasaki, Japan*
[3]*Laboratory for Medical Engineering, Division of Materials, Science and Chemical Engineering, Graduate School of Engineering, Yokohama National University, Yokohama, Japan*

BACKGROUND. Obesity is known to be associated with prostate cancer development and progression, but the detailed mechanism is not clear. Monocyte chemotactic protein-1 (MCP-1) is secreted from cancer cells, stromal cells, and adipocytes, and it is involved in prostate cancer progression. Here we investigated the biological role of MCP-1 secreted from adipocytes for prostate cancer cells.

METHODS. Human pre-adipocytes (HPAds) were cultured and differentiated to mature adipocytes. Conditioned medium (CM) from HPAd cells was obtained using phenol red-free RPMI1640 medium. We performed a cytokine membrane array analysis to detect cytokines in the CM. To characterize the physiological function of MCP-1 in the CM, we performed an MTT-assay, a wound-healing and invasion assay with anti-MCP-1 antibody using three prostate cancer cell lines: DU145, LNCaP, and PC-3. Matrix metalloproteinase (MMP)-2 and MMP-9 activities were evaluated by gelatin zymography. A qPCR and Western blotting were used to examine the mRNA and protein expression levels of MMP-2.

RESULTS. The cytokine membrane array of the CM showed a strong signal of MCP-1compared to the control medium, and we thus focused our attention on MCP-1 in the CM. The CM up-regulated the cancer cell proliferation, and the neutralization by anti-MCP-1 antibody inhibited the proliferative effect of the prostate cancer cell lines. The CM greatly increased the invasive activity in the prostate cancer cell lines, and anti-MCP-1 antibody decreased the invasiveness. Gelatin zymography revealed that the CM markedly enhanced the enzymatic activity of MMP-2, and anti-MCP-1 antibody down-regulated its effect. MMP-2 mRNA expression was undetected and the MMP-2 protein level was unchanged between the control medium and CM in DU145 cells.

CONCLUSIONS. MCP-1 from adipocytes enhances the growth and invasion activity of prostate cancer cells. The inhibition of MCP-1 derived from adipocytes might be an effective treatment for prostate cancer. *Prostate 75:1009–1019, 2015.* © 2015 Wiley Periodicals, Inc.

KEY WORDS: **prostate cancer; adipocyte; MCP-1; invasion; MMP-2**

Grant sponsor: JSPS KAKENHI; Grant numbers: 25462493; 26670709; Grant sponsor: Regional Innovation Strategy Support Program of MEXT.
Yusuke Ito and Hitoshi Ishiguro contributed equally to this work.
Conflict of interest: The authors declare no conflict of interest.

*Correspondence to: Hiroji Uemura, Department of Urology, Yokohama City University Graduate School of Medicine, 3-9 Fukuura, Kanazawa-ku, Yokohama 236-0004, Japan. E-mail: hu0428@med.yokohama-cu.ac.jp

Received 10 November 2014; Accepted 6 January 2015
DOI 10.1002/pros.22972
Published online 27 April 2015 in Wiley Online Library (wileyonlinelibrary.com).

INTRODUCTION

The numbers of prostate cancer patients have been increasing in Japan and western countries [1]. The mechanisms of prostate cancer progression are explained by androgen receptor and oncogenes' mutations and amplification, inhibition of tumor suppressor genes, and abnormalities of many growth factors and cytokines [2]. Growth factors and cytokines are supplied to prostate cancer cells not only in an autocrine manner but also in a paracrine manner [3]. Environmental factors are also involved in prostate cancer development and progression [4].

Among these environmental factors, diet is known to change gene expressions and induce prostate cancer development [5,6]. High-fat diets induce obesity, which leads to an elevated incidence of aggressive prostate cancer [7,8]. Prostate cancer patients with obesity have worse prognoses and a tendency to progress to a higher stage [7]. The prostate cancer-related death ratio was also found to be higher in obese men compared to non-obese men [8]. Obesity thus has some responsibility for prostate cancer progression. However, the detailed molecular mechanisms underlying the progression of prostate cancer as affected by obesity are unknown.

Adipocytes are known to have various functions for the growth, migration, and invasion of surrounding cells by their secretion of growth factors and cytokines. For example, leptin, one of the cytokines secreted by adipocytes, is elevated in obesity and exerts a pro-tumor effect in human prostate cancer cell lines [9–11]. Thus, cytokines related to obesity may also share responsibility for prostate cancer development and progression.

In the present study, we assessed the growth factors and cytokines secreted by adipocytes and investigated the relationship between adipocytes and prostate cancer progression. The results of a cytokine array in the conditioned medium (CM) of adipocytes showed that monocyte chemotactic protein-1 (MCP-1) was greatly elevated. Our results suggest that MCP-1 secreted from adipocytes regulates both prostate cancer progression and the enzymatic activation of matrix metalloproteinase (MMP)-2.

MATERIALS AND METHODS

Prostate Cancer Cell Lines

LNCaP, PC-3, and DU145 cells were obtained from the American Tissue Culture Collection (Rockville, MD). Each cell was maintained in F-12 (for LNCaP and PC-3) or MEM (for DU145) medium supplemented with 10% heat-activated fetal bovine serum (FBS) under 5% CO_2 at 37°C. In the experiments, these cells were starved using phenol red-free RPMI1640 medium for 48 hr and then used for the stimulation experiments.

Differentiation of Adipocytes and Preparation of the Conditioned Medium (CM)

Human pre-adipocytes (HPAds) were obtained from Cell Applications (San Diego, CA). Cells in 75 cm^2 flasks were maintained in pre-adipocyte basal medium with growth supplement at 37°C under 5% CO_2. When the cells had grown to 4.0×10^4 cells/cm^2, the medium was changed to adipocyte differentiation medium (ADM) for cell differentiation to mature adipocytes. The ADM was changed every other day for a week. Cell differentiation was confirmed by the staining of fat drops using Oil-Red-O (Sigma–Aldrich, St. Louis, MO).

For the conditioned medium (CM) preparation, mature adipocytes were washed in phosphate-buffered saline (PBS), and then 15 ml phenol-red free RPMI1640 medium was added to the flask. After 24-hr incubation, the medium was centrifuged to remove cells and stored at −80°C until the experiments. Phenol red-free RPMI1640 medium without FBS was used as the control medium for all experiments.

Cytokine Membrane Array

Cytokines and growth factors present in the CM and in the control medium were detected using the Ray Bio Human Cytokine Antibody Array III kit (RayBiotech, Norcross, GA) according to the manufacturer's instructions. Briefly, after each membrane was blocked by blocking buffer, 1 ml of CM or control medium was added to each membrane and the membranes were then incubated overnight at 4°C. The next day, the membranes were washed five times with washing buffer and incubated with 1 ml of the Biotinylated Antibody Cocktail for 2 hr at room temperature (RT). After the membranes were washed, 2 ml of HRP-Streptoavidin were added and the membranes were incubated for 2 hr at RT and washed again. Signals for growth factors and cytokines were detected using the ImageQuant LAS 4000 imaging system (Fujifilm, Tokyo).

MCP-1 ELISA

MCP-1 in the CM and control medium was measured using a Quantikine human CCL2/MCP-1 ELISA kit (R&D Systems, Minneapolis, MN) according to the manufacturer's instructions. Briefly, 200 µl of each sample was added into each well of MCP-1 microplate and incubated for 2 hr at RT. After the wells were washed three times with washing buffer,

the plate was incubated with 200 μl of MCP-1 conjugate for 1 hr at RT. Then, 200 μl of Substrate Solution (R&D Systems) was added to each well and the plate was incubated for 30 min at RT. The reactions were stopped by adding 50 μl of stop solution, and the optical density was determined using a microplate reader (TECAN infinite F200 PRO, Tecan Group, Männedorf, Switzerland) set to 450 nm.

Cell Growth

Cell growth was measured by a direct cell count or an MTT assay. For the cell count assay, each cell (LNCaP; 4×10^4 cells/well, DU145; 1×10^4 cells/well) were seeded in 12-well plates. After the stimulation, cells were washed with PBS, trypsinized and counted using the Z1 Coulter Particle Counter (Beckman Coulter, Brea, CA). For the MTT assay, each cell (LNCaP, 8×10^3cells/well; DU145 and PC-3, 5×10^3 cells/well) were seeded in 96-well plates. After the cells were incubated 24 hr, they were starved and stimulated with CM or control medium, and with MCP-1. Finally, 10 μl TetraColorOne (Seikagakukogyo, Tokyo) was added to each well and absorbance was quantified with the manufacturer's procedures.

In the case of the experiments using anti-MCP-1 antibody (#23007, R&D Systems), the cells were treated with antibody before the stimulation.

Real-Time Quantitative Polymerase Chain Reaction (RT-qPCR)

Total RNA from cells and prostate cancer tissues was extracted using ISOGEN (Nippon Gene, Toyama, Japan). cDNA was synthesized using 1 μg total RNA and the High Capacity cDNA Reverse Transcription kit (Applied Biosystems/Life Technologies, Carlsbad, CA) with random hexamers, according to the manufacturer's instructions. Real-time quantitative polymerase chain reaction (RT-qPCR) was carried out using a Taqman Fast Advanced Master Mix on the StepOnePlus™ Real Time PCR System (Applied Biosystems/Life Technologies). All target gene Taqman primers and probes were purchased commercially (Applied Biosystems/Life Technologies). The reactions were performed for 20 sec at 95°C for pre-heating, then 1 sec at 95°C, 20 sec at 60°C for 40 cycles. The expression levels were calculated using the $2^{-\Delta\Delta Ct}$ method. β-actin was used as an endogenous control for all gene expression analyses.

Wound-Healing Assay

Cells (1.0×10^5 cells/well) were seeded into 12-well plates. At 48 hr after seeding, the medium was changed to phenol red-free RPMI1640 medium. After a 6-hr incubation, the confluent monolayer cells were gently scratched with a pipette yellow tip to create a cell-free straight area in the center of the dishes. One milliliter of CM or control medium with or without anti-MCP-1 antibody was added to each well. Just after scratching and after 12-hr migration, the cells were observed with a phase-contrast inverted microscope and photographed. The breadth of the scratched lane was measured at three points for each well using Image J software ver. 1.46r and then averaged for each well. The wounded area after 12-hr incubation was calculated according to the formula: (mean wounded breadth − mean remained breadth)/mean wounded breadth × 100 (%).

Invasion Assay

Cell invasion was investigated using Biocoat matrigel invasion chambers with 8-μm pore polycarbonate membranes that had been pre-coated with Matrigel (BD Biosciences, San Jose, CA). After the chambers were rehydrated, 2.5×10^4 cells in 500 μl of control medium were transferred to the upper chamber. The lower chambers were filled with CM or control medium. The cells were allowed to incubate for 24 hr, and the invading cells on the lower surface of the insert were fixed and stained with Diff-Quik (Sysmex, Hyogo, Japan). All invading cells in the whole insert were counted (n = 4). Experiments were repeated three times, and the results were the averages of the three independent experiments.

Western Blot Analysis

Cells treated with CM or control medium with anti-MCP-1 antibody were washed in ice-cold PBS and then dissolved in RIPA buffer (R0278; Sigma–Aldrich) with protease inhibitor cocktail (P8340; Sigma–Aldrich) and phosphatase inhibitor cocktails (P2850, P5726; Sigma–Aldrich). The lysate was centrifuged for 30 min at 15,000 × *g* at 4°C, and the supernatant was harvested as samples.

After determination of the protein concentration using the Bio-Rad protein assay (Bio-Rad, Hercules, CA), 20 μg of the total cell lysate was electrophoresed by Sodium dodecyl sulfate-polyacrylamide gel electrophoresis (SDS-PAGE) and electrophoretically transferred to Immobilon-P membranes (Millipore, Billerica, MA). After the transferred membranes were blocked using the blocking reagent N102 (NOF Corp., Tokyo), they were incubated overnight at 4°C with specific antibodies in Tris buffered-saline containing Tween 20 (TBST; 150 mM NaCl, 20 mM Tris, and 0.05% Tween 20).

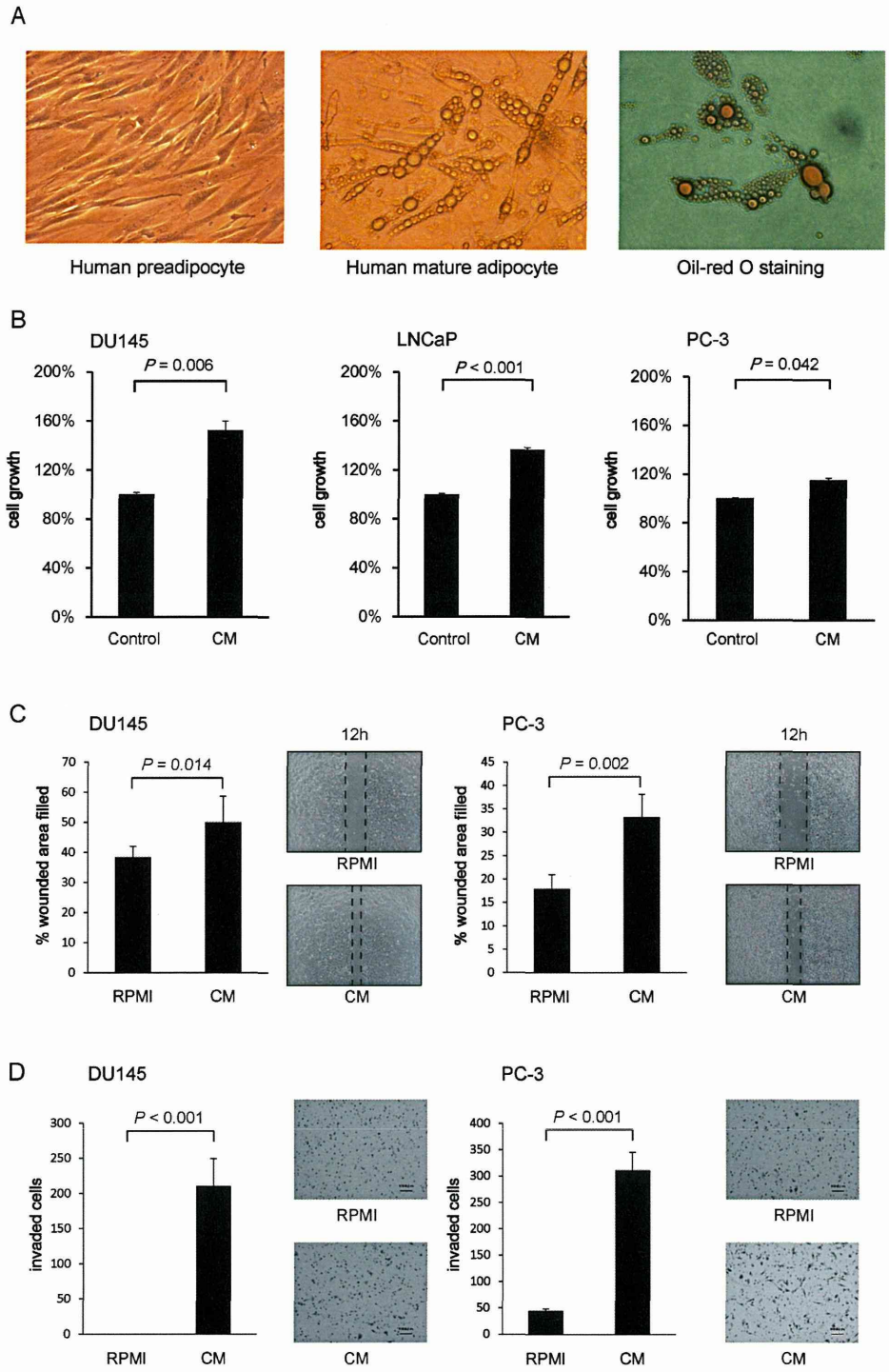

Fig. 1. The CM induced prostate cancer cell progression. (**A**) Representative photos before and after the differentiation of adipocytes. Cells were differentiated to mature adipocytes and confirmed by the staining of fat drops using Oil-red O. (**B**) An MTT assay was performed and cells were counted 48 hr after stimulation with CM. Each cell (LNCaP, 8×10^3 cells/well; DU145 and PC-3, 5×10^3 cells/well) were seeded, and all experiments were repeated three times. (**C**) The migration activity of DU145 and PC-3 cells was measured in a wound-healing assay. Just after being scratched and after 12 hr migration, the cultures were photographed. The wounded area after 12-h incubation was calculated as described in the Materials and Methods. (**D**) The invasion activities of DU145 and PC-3 cells were measured by a transwell invasion assay. Each well was seeded and incubated for 24 hr, and all invading cells were counted.